Defect Profiling of Oxide-Semiconductor Interfaces Using Low-Energy Muons

Maria Mendes Martins,* Piyush Kumar, Judith Woerle, Xiaojie Ni, Ulrike Grossner, and Thomas Prokscha

Muon spin rotation with low-energy muons (LE-μSR) is a powerful nuclear method where electrical and magnetic properties of surface-near regions and thin films can be studied on a length scale of $\approx$200 nm. This study shows the potential of utilizing low-energy muons for a depth-resolved characterization of oxide-semiconductor interfaces, i.e., for silicon (Si) and silicon carbide (4H-SiC). The performance of semiconductor devices relies heavily on the quality of the oxide-semiconductor interface; thus, investigation of defects present in this region is crucial to improve the technology. Silicon dioxide (SiO_2) deposited by plasma-enhanced chemical vapor deposition (PECVD) and grown by thermal oxidation of the SiO_2-semiconductor interface are compared with respect to interface and defect formation. The nanometer depth resolution of LE-μSR allows for a clear distinction between the oxide and semiconductor layers, while also quantifying the extension of structural changes caused by the oxidation of both Si and SiC. The results demonstrate that LE-μSR can reveal unprecedented details on the structural and electronic properties of the thermally oxidized SiO_2-semiconductor interface.

1. Introduction

At present, silicon (Si) is still the most commonly used semiconductor for most applications. However, high expectations are raised by silicon carbide (4H-SiC), a wide-bandgap semiconductor exhibiting a high breakdown voltage and thermal conductivity, but also high chemical stability.[1] Being a robust and biocompatible material that can sustain harsh environments, SiC is also used in the biomedical field.[2] More recently, SiC proved to be a

promising platform for quantum technologies, with implementation, as single photon emitter, for quantum communication and sensors.[3,4] With respect to other semiconductors, an advantage of Si and SiC is their ability to form native silicon dioxide (SiO_2). Silicon dioxide is an excellent insulator with a large dielectric strength and high temperature stability. It is also inert to most chemicals, can act as a diffusion barrier, and since it is easy to grow, etch, and pattern, it plays a crucial role in most device manufacturing processes. For many applications, the growth of a high-quality oxide-semiconductor interface with low densities of defects is critical. Over the past decades, continuous efforts have been placed in optimizing oxidation processes for better device performance and reliability. However, despite the tremendous progress in improving the quality of the SiO_2/Si and SiO_2/SiC interfaces, the characterization and understanding of oxidation-induced defects - both in the oxide and the semiconductor - remain challenging.

Electrical properties of oxide-semiconductor interfaces are commonly obtained using capacitance-voltage (C–V) or conductance-voltage (G–V) measurements of metal-oxide-semiconductor (MOS) structures.[5,6] These techniques allow for a very accurate determination of the energy position of oxide or interface defects, however, the information obtained on the defect's nature or their spatial distribution with respect to the interface is very limited.

Based on angle-resolved X-ray photoemission spectroscopy, transmission electron microscopy and electron-energy-loss-spectroscopy, it is commonly assumed that the majority of defects are located in the narrow transition region between the semiconductor and the oxide and that there is a direct correlation between the width of this transition region and the performance of the MOS devices. However, there is a large spread of experimental data on the extension of this sub-stoichiometric region, ranging from several Å to tens of nm,[7–10] and an unambiguous interpretation of the structural information is not always available.

A powerful technique for the investigation of semiconductor defects is muon spin rotation spectroscopy (μSR),[11,12] an atomic, molecular, and condensed matter experimental

M. Mendes Martins, P. Kumar, J. Woerle, U. Grossner
Advanced Power Semiconductor Laboratory
ETH Zurich
Physikstrasse 3, Zurich 8092, Switzerland
E-mail: maria.martins@psi.ch

M. Mendes Martins, X. Ni, T. Prokscha
Laboratory for Muon Spin Spectroscopy
Paul Scherrer Institute
Forschungsstrasse 111, Villigen PSI 5232, Switzerland

technique based on nuclear detection methods. The technique usually uses a beam of spin-polarized, positively charged muons, unstable elementary particles with a lifetime of 2.2 μs. The muons are implanted into the target material, where they act as a sensitive probe for their local electronic and magnetic environment before decaying into a positron and two neutrinos. The decay positron is anisotropically emitted, preferentially in the direction of the muon spin at the time of decay, and is detected by an array of scintillators placed around the sample chamber. The decay asymmetry $A(t)$ is the signal obtained from the recorded decay positrons along the different detection directions, and determines the time evolution of the muon spin ensemble polarization. When the muon is implanted in insulators and semiconductors, it can thermalize as an unbound muon, or it can pick up one or even two electrons forming different muonium configurations (Mu^+, Mu^0, and Mu^-). Since the Mu states are very sensitive to interaction with charge carriers and defects, the formation probability of each Mu state is strongly dependent on its local surroundings.[13–18] In μSR, neutral and charged muonium states can be identified by the spin precession frequency in an applied magnetic field: Mu^+, like a free muon, will have a spin precession equal to the muon's Larmor frequency, while Mu^0 has a faster precession (about 103 times in a low magnetic field in the order of mT) due to the strong hyperfine coupling between the muon and the electron. The other charged state, Mu^-, is indistinguishable from $μ^+$ by spectroscopic methods, because the hyperfine coupling of the muon with the two electrons with opposite spin cancels. The charged $Mu^{+/-}$ configurations are called diamagnetic states, to distinguish them from the paramagnetic Mu^0 state.

Low-energy (LE) μSR is a compelling extension to conventional bulk μSR which allows studying thin samples and multi-layered structures with a depth-resolution of a few nanometers.[19] Low-energy muons are obtained by the moderation of typically 4 MeV muons to almost thermal energies and subsequent acceleration by an electrostatic field.[20–23] By varying the energy in the range of 1 to 25 keV, one can control the mean stopping depth of the muons. Depending on the material, it is possible to probe specific regions close to the surface and interfaces in a depth-resolved manner up to a depth of about 200 nm.

Recently, LE-μSR was successfully used to study defects and band-bending effects near the surface in a variety of semiconductors such as Si, SiC, Ge, CdS, or ZnO.[18,24–27] For example, LE-μSR investigations of p-type Ge allow the direct observation of majority charge-carrier profiles in the near-surface region which is changed by external illumination with a blue laser ($\lambda = 457$ nm).[18] Initially, depletion of holes is observed near the surface due to charged surface states, and as the sample is illuminated, photogenerated electrons occupy empty surface acceptor states and attract holes into the hole depletion layer. LE-μSR has also been successfully deployed to obtain the profile of defects in the near-surface region of SiC, where the suppression of Mu^0 formation is attributed to the presence of defects in the crystal.[24] In particular, the μSR signal shows a distinct behavior for samples with large densities of either carbon or silicon vacancies.[25] Here, the interaction of the $μ^+$ with Si vacancies favors the formation of Mu^0, while the C vacancy center prompts an electron double capture to form Mu^-, resulting in an enhanced diamagnetic signal.

Table 1. Si n-type samples with donor concentration N_D, oxide thickness t_{ox}, and density of interface states D_{it}. All samples are cut from the same (100) Si wafer.

Name	Crystal Orientation	N_D (cm^{-3})	Oxidation Process	t_{ox} (nm)	D_{it} (cm^{-2} eV^{-1})
Si-A	(100)	5×10^{16}	PECVD	105	9×10^{11}
Si-B	(100)	5×10^{16}	thermal	110	2×10^{12}
Si-C	(100)	5×10^{16}	thermal, HF, PECVD	95	–

Table 2. SiC n-type samples with donor concentration N_D, oxide thickness t_{ox}, and density of interface states D_{it}. All samples are cut from the same 4H-SiC wafer with a low-doped epitaxial layer on the Si-face and the highly doped substrate on the C-face.

Name	Crystal Orientation	N_D (cm^{-3})	Oxidation Process	t_{ox} (nm)	D_{it} (cm^{-2} eV^{-1})
SiC-A	(0001) Si	8×10^{15}	PECVD	105	1×10^{12}
SiC-B	(0001) Si	8×10^{15}	thermal + PECVD	30 + 70	8×10^{12}
SiC-C	(000$\bar{1}$) C	$\approx 1 \times 10^{19}$	thermal	85	–
SiC-D	(000$\bar{1}$) C	$\approx 1 \times 10^{19}$	thermal, HF, PECVD	95	–

In this study, we take advantage of the superior nanometer depth-resolution of LE-μSR to investigate interfacial systems, with focus on the muon probe response to either thermally grown or deposited SiO_2 on both Si and 4H-SiC. The chosen set of samples intends to give insight into the defects formed in the SiO_2/semiconductor systems by oxidation, and how this could impact devices. Differences in both the oxide and the interface quality after the two oxidation treatments are observed, where the LE-μSR data reveal a 10 to 30 nm wide interface region with enhanced defect density at the thermally grown SiO_2/Si and SiO_2/4H-SiC interfaces. At the SiO_2/semiconductor interfaces, the diamagnetic signal is sensitive to changes in defect and charge carrier concentrations, which depend on the distinct oxidation processes and the initial doping concentrations of the semiconductors. LE-μSR allows for the first time to determine the range of enhanced defect and modified carrier concentrations at the interfaces, with a depth resolution of a few nanometers.

2. Results and Discussion

An overview of the investigated samples for this LE-μSR study is given in **Tables 1** and **2**. A SiO_2 film was formed on all samples, either by a low-temperature deposition in a plasma–enhanced chemical vapor depositions (PECVD) chamber or by thermal growth in O_2 ambient. As the focus of this study was the investigation of interface defects and their effect on the LE-μSR signal, no post-oxidation annealing treatment was performed for any of the samples. A thickness of the SiO_2 layers of about 100 nm has been chosen for all samples to allow for probing the interface regions with the same implantation energies. The stopping profiles of the muons are simulated for each sample using the TRIMSP code,[28,29] and provide the mean stopping depth of the muon beam for a given implantation energy. The stopping profiles are calculated based on the density of the two oxides, measured with X-ray reflectivity, and are presented for three of the samples in **Figure 1**. For muon implantation energies <10 keV, the oxide layer is probed, while energies >16 keV mainly probe the
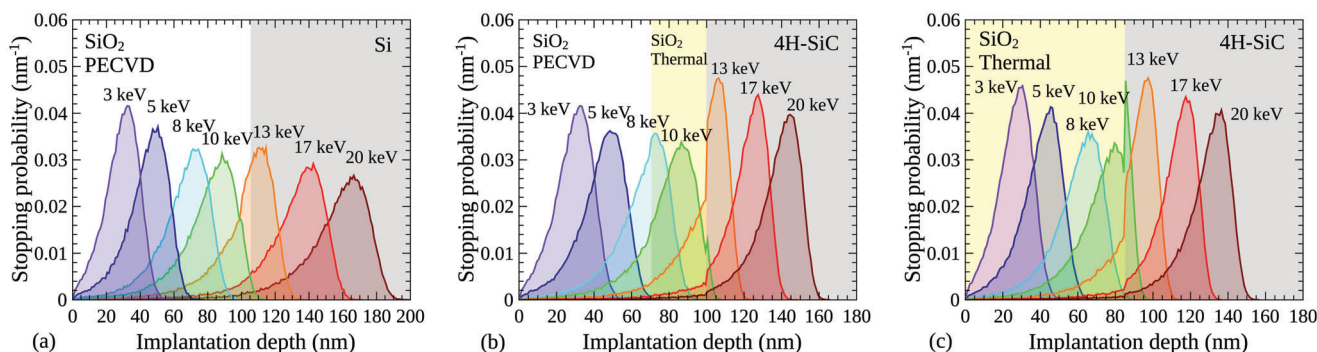
**ADVANCED
SCIENCE NEWS**

www.advancedsciencenews.com

**ADVANCED
MATERIALS
INTERFACES**
Open Access

www.advmatinterfaces.de

Figure 1. Simulated stopping profiles for three of the studied oxide-semiconductor samples obtained with TRIMSP. a) Si-A with a PECVD oxide of 105 nm. b) SiC-B with both a thin thermally grown (30 nm) and a deposited SiO_2 (70 nm), on top of 4H-SiC. c) SiC-C with 85 nm thermally grown SiO_2 layer on top of 4H-SiC.

semiconductor bulk. Implantation energies between these two values are used to study the interface and near-interface region.

In µSR, the so-called dia- and paramagnetic decay asymmetries A_D and A_{Mu}, are determined by the amplitudes of the muon spin precession signals in an applied magnetic field transverse to the initial muon spin direction (transverse-field TF-µSR). The experimental data were recorded at two magnetic fields - 0.5 and 10 mT - whereby the precession frequency of the paramagnetic signal at 10 mT is too high to be observed with the time resolution of the instrument (see Experimental Section). The measured asymmetries are proportional to the fraction of muons in the particular state. The respective fractions are calculated as: $F_D = A_D/A_{total}$, and $F_{Mu} = 2 \cdot A_{Mu}/A_{total}$, where A_{total} is the maximally observable decay asymmetry of the µSR spectrometer. The factor of 2 in F_{Mu} accounts for the fact that only 50% of the total Mu^0 polarization is observable in our experiment with an applied magnetic field of 0.5 mT.[11] If no Mu^0 is formed, the diamagnetic fraction F_D is one. Smaller values - normally observed in insulators and semiconductors - indicate the formation of Mu^0. At low temperatures and moderate doping of the semiconductor, more than 90% of the implanted μ^+ are expected to form such a paramagnetic state in Si and 4H-SiC.[25,30] Very often, some fraction of Mu^0 states formed in insulators or semiconductors does not contribute to the precession signal due to fast muon spin depolarization processes, leading to a reduction of A_{Mu} and to the observation, that, in general, $F_D + F_{Mu} \leq 1$ (which is called the *missing fraction* of muon spin polarization in µSR).[14] The fraction of muons forming each state is sensitive to its environment and to the presence of defects. Thus, by measuring F_D and F_{Mu} as function of depth x, changes in defect and charge carrier concentration can be determined with nanometer resolution while crossing the interface. The depth dependence of $F_D(x)$ and $F_{Mu}(x)$ was obtained from the correlation between the implantation energy of the muon and mean stopping depth illustrated by the stopping profiles, with the fitting procedure detailed in Section 4. Since the measured fractions, depend on the physical environment where the muon stops, the fit model assumes F_D and F_{Mu} to be constant within each layer, and changing abruptly at the interface of two layers. Depending on the sample preparation methods, the muons may be sensitive to regions with different properties, and the extensions of these regions can be extracted by considering additional layers in the model. As will be discussed below, for the deposited

SiO_2 samples, the fit result is consistent with the measured thickness of the oxide, highlighting the accuracy of the analysis.

2.1. The SiO_2/Si Interface

The results of the LE-µSR measurements ($F_D(E)$) at 10 mT for the SiO_2/Si interface are summarized in **Figure 2** a–c and corresponding fit results $F_D(x)$ are shown in Figure 2d–f. The vertical dotted lines represent the uncertainty in determining the exact interface position by profilometer and X-ray reflectivity measurements. Additionally, for Si-A and Si-B, F_{Mu} was extracted from the 0.5 mT measurements and is shown in Figure 2g–h.

In SiO_2, typically more than 60% of the muons form Mu^0, and almost 30% of the implanted muons decay in the diamagnetic state.[31–33] In PECVD-grown SiO_2 (Figure 2a), the diamagnetic fraction is about 50%, possibly due to electron trapping in the low quality oxide, as hinted by the suppression of Mu^0 formation (Figure 2g).[24,27] In the case of the thermally grown oxide shown in Figure 2b, the diamagnetic fraction for low implantation energies is significantly lower than for the deposited oxide and comparable to what was previously reported for SiO_2 crystal or glass.[32] Measurements at 0.5 mT show a F_{Mu} of 65% (Figure 2h) indicating an undisturbed Mu^0 formation process in the SiO_2, and a higher structural order of SiO_2.

Another remarkable difference between the oxidation processes is the effect of each one has on the interface formed with the semiconductor. The PECVD-SiO_2 can be clearly distinguished from Si in the LE-µSR signal, as F_D quickly drops to the Si bulk value at the interface of samples Si-A and Si-C (Figure 2d,f). For sample Si-B with a thermally grown oxide, F_D increases around the SiO_2/Si interface, suggesting a defect-rich region that affects the SiO_2 layer ($\approx$20 nm) and the near-interface region of Si (5 to 10 nm). On the Si side, besides the presence of defects or structural disorder, the increase of F_D could also be explained by electron accumulation in the interface region.[18] In SiO_2, the existence of a defect-rich region is further supported by the fast drop of F_{Mu} in Figure 2h, where a conversion of Mu^0 to the diamagnetic state occurs at a muon implantation energy of 10 keV, corresponding to a probing depth of $\approx$20 nm away from the interface toward the oxide side. Extraction of D_{it} in Table 1, reveals fairly large D_{it} values for the thermally grown oxide
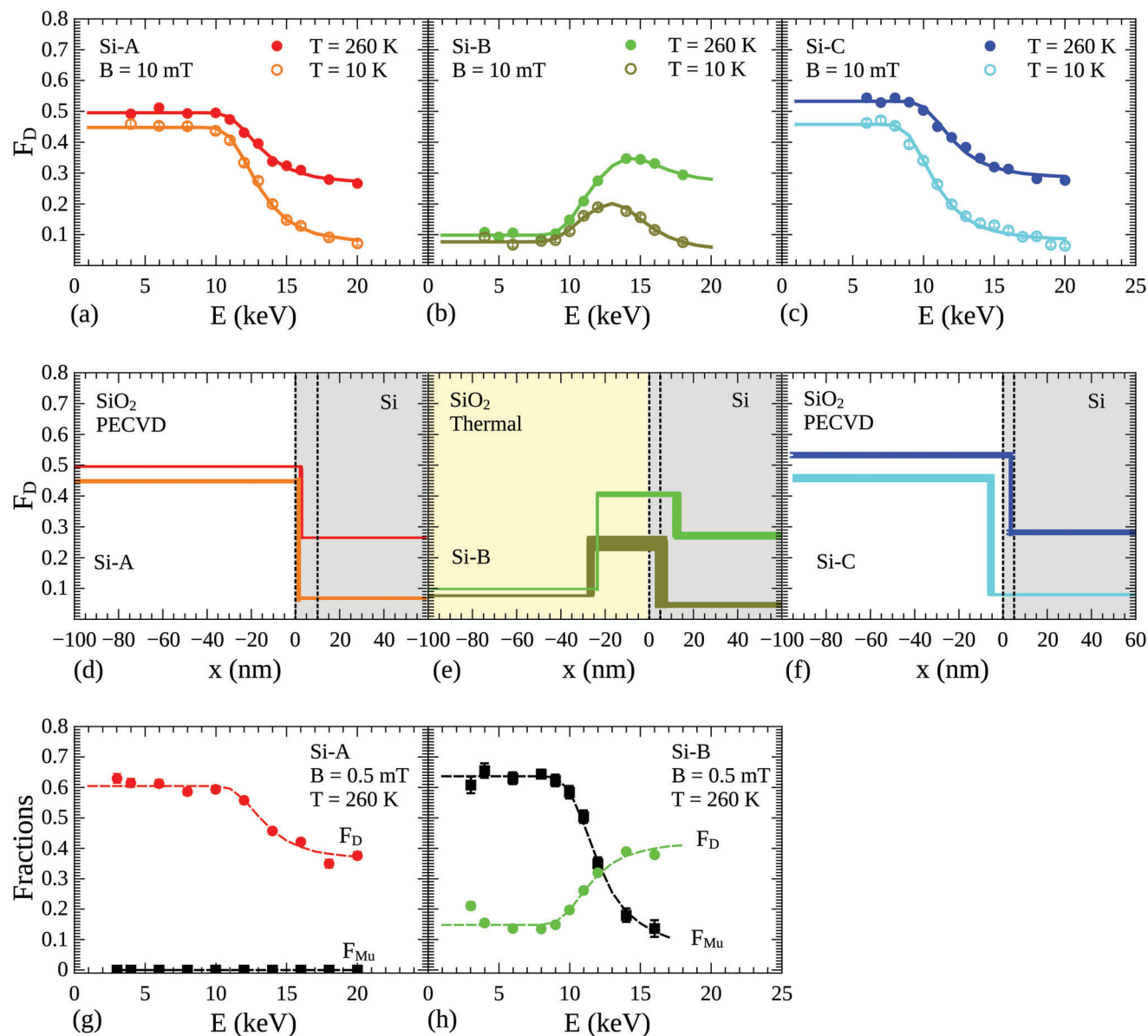
Figure 2. Analysis of diamagnetic (F_D) and paramagnetic (F_{Mu}) fractions measured in the Si samples. a–c) F_D as function of muon implantation energy measured at 10 and 260 K with an externally applied magnetic field of 10 mT. d–f) Depth variation of F_D obtained by fitting the corresponding muon implantation energy dependence. The width of the colored lines indicates the standard deviation of the fit parameters. g–h) F_D and F_{Mu} as function of muon implantation energy measured at 0.5 mT. The fitted dashed lines describe the variation of the fractions, assuming $F_D(x)$ and $F_{Mu}(x)$ are abruptly changing between the different layers of the sample.

(2×10^{12} cm^{-2} eV^{-1}) and the deposited oxide (9×10^{11} cm^{-2} eV^{-1}), which is expected for oxidation processes without any further annealing treatments.[34,35] However, this also implies that the observed increase of F_D around the interface of the thermally grown oxide (Si-B) can not solely be explained by the presence of dangling bonds at the SiO$_2$/Si interface.[6,7] Instead, one has to consider a combination of factors, including oxide charges and interface traps in the SiO$_2$, and at the interface, point defects and charge accumulation in the Si as well as strain-induced lattice distortions across the interface.[36,37]

Although the oxidation-induced strain is expected to quickly relax away from the interface, stress-related lattice distortion may

contribute to the observed reduction of F_{Mu} in Figure 2h. On the Si side, this strain-induced reduction of F_{Mu} cannot be separated from the fast depolarization of Mu^0 in Si due to the presence of free electrons/dopants with $N_D = 5 \times 10^{16}$ cm^{-3},[14] as the detection of strain-induced effects on F_{Mu} would require a Si sample with $N_D < 10^{13}$ cm^{-3} to significantly reduce the depolarization of Mu^0 caused by the presence of charge carriers.

When removing the thermally grown SiO$_2$ from the Si sample and depositing a PECVD-SiO$_2$ instead (Figure 2c), the defective region around the interface disappears and a very similar F_D as for sample Si-A is observed. Interestingly, without the thermal oxide, the F_D on the Si side also recovers to the same values as

**ADVANCED
SCIENCE NEWS**

www.advancedsciencenews.com

**ADVANCED
MATERIALS
INTERFACES**
Open Access

www.advmatinterfaces.de

for the deposited oxide, suggesting that the Si is not permanently altered by the thermal oxidation.

At energies $\gtrsim 16$ keV where the Si bulk is probed, all three samples show similar diamagnetic fractions of $\approx 10\%$ and $\approx 27\%$ for temperatures $T = 10$ and 260 K, respectively, indicating that the Si remains unchanged from the oxidation process at these depths. The larger value of F_D at $T = 260$ K is a result of the thermally activated ionization of one of the two Mu^0 states in Si: Mu^0 can either form at the bond-center between two Si atoms (Mu_{BC}), or at the tetrahedral interstitial site (Mu_T).[14,30] It is the Mu_{BC} state with a fraction of $\approx 30\%$ which ionizes at $T > 150$ K to form the diamagnetic Mu_{BC}^+ state,[30,38,39] which causes the observed increase of F_D at 260 K.

2.2. The SiO_2/4H-SiC Interface

A summary of the processing parameters of the SiC samples is given in Table 2. Here, we also studied how the doping concentration and crystal orientation of the semiconductor impacts the F_D and F_{Mu} formation process across the interface. While the SiO_2/SiC interface was formed on the low-doped (0001) Si-face for samples SiC-A and SiC-B, measurements on samples SiC-C and SiC-D were performed on the highly doped (000$\bar{1}$) C-face. As the oxide growth rate at 1050 °C for (0001) 4H-SiC is too low to achieve the targeted oxide thickness of 100 nm, only a 30 nm thick oxide was thermally grown on sample SiC-B and a 70 nm-thick PECVD-SiO_2 was deposited on top. The sample SiC-D first had a thermal oxide, which was removed and a PECVD-SiO_2 was deposited, to investigate any permanent change of the SiC due to thermal oxidation.

Figures 3 a–c) and **4**a show $F_D(E)$ measured on the 4H-SiC samples at an applied magnetic field of 10 mT, with the corresponding fit results for $F_D(x)$ in Figures 3d–f) and 4b. The diamagnetic and paramagnetic fractions, measured at 0.5 mT, are presented in Figure 3g–i). Again, the vertical dotted lines represent the uncertainty in determining the exact interface position by profilometer and X-ray reflectivity measurements. As before for the Si samples, the depth-dependence of $F_D(x)$ in Figure 3d–e) clearly indicates the SiO_2/SiC interface where F_D quickly changes to the typical 4H-SiC bulk value.[24,25]

The PECVD oxide of samples SiC-A, SiC-B, and SiC-D show a similar behavior as on Si with a strong increase of F_D compared to the bulk thermal oxide and a suppression of Mu^0 formation across the whole oxide layer. Similar to Si-B, the thermal oxide in the SiC-B and SiC-C samples has a higher structural order compared to PECVD-SiO_2, allowing observation of the Mu^0 precession in the SiO_2 layers. This is also supported by the D_{it} analysis, revealing a larger density of interface states (8×10^{12} cm^{-2} eV^{-1}) for the thermally grown oxide (SiC-B) compared to the Si samples or the deposited SiO_2 on SiC-A (1×10^{12} cm^{-2} eV^{-1}). Thermal oxidation of Si and SiC is very similar, however, in the case of SiC, it does not only involve the formation of bonds between Si and O, but also diffusion of C.[40,41] If the carbon atoms are not efficiently removed from the interface, they may form carbon-related defects directly at, or in the vicinity of the SiO_2/SiC interface.[42] Hence, apart from dangling bonds, interfacial carbon clusters, and near-interface oxide traps are expected to contribute to the interface defect state density.[43] Addi-

tionally, out-diffusion of Si from the SiC bulk and the generation of silicon vacancies contribute to the increase in defect concentrations close to the SiO_2/SiC interface.[44,45] The Si out-diffusion during thermal oxidation leads to a C-rich surface where large areas of graphene-like monolayers are likely to form.[46] For the SiC samples discussed here, the D_{it} analysis revealed a larger interface defect density ($D_{it} = 8 \times 10^{12}$ cm^{-2} eV^{-1}) for the thermally grown oxide of sample SiC-B compared to the Si samples or the deposited SiO_2 on sample SiC-A ($D_{it} = 1 \times 10^{12}$ cm^{-2} eV^{-1}). Although Mu^0 is visible in the thermal-SiO_2 layer of Si-face SiC (Figure 3h), the F_D of 22% inside the SiO_2 layer (Figure 3e) is comparable to the value measured at 10 K in the defective SiO_2 region near the interface of Si-B (Figure 2e), thus evidencing the enhanced defect concentration in the thermally grown SiO_2 layer of SiC-B and oxidation-induced strain.[47]

2.2.1. Impact of Crystal Orientation

The quality of the SiO_2/SiC interface also depends on the polarity of the oxidized SiC face. For the C-face, the thermal oxidation process using the same parameters is almost ten times faster than for the Si-face.[48] Thus, the thermal oxide process results in a 90 nm thermal-SiO_2 layer on the C-face in SiC-C. A region with enhanced F_D formation appears near the interface in the SiO_2-layer, as in Si-B and SiC-B. This oxide defective region in SiC-C is narrower than in SiC-B, and affects only 10 to 15 nm (Figure 3f), which suggests less induced strain for SiO_2 layers grown on the C-face.[49] However, as compared to Si-B and SiC-B, the higher value of F_D in the interface region of the oxide suggests the presence of a much higher D_{it} for SiO_2 thermally grown on the C-face.[50,51] For the C-face samples measured with LE-μSR, it was not possible to extract D_{it} due to the high doping density of SiC, which led to very high leakage current, and the surface potential of the semiconductor couldn't be varied with external bias. The defective region in SiC for the Si-face is 5 nm, much narrower than for C-face sample, which is 30 nm. These values were extracted from the 10 K measurements, where freeze-out of charge carriers occurs. This difference can be attributed to the different ways of graphitization of the Si- and C-face. At the Si-face, only monolayers of graphene are expected to form at temperatures below 1250 °C, whereas the C-face graphitizes already at lower temperatures and generates multilayers of graphene.[52,53] Thus, the 30 nm wide region (Figures 3f and 4b) with a sharp rise in F_D observed in C-face face samples (SiC-C and SiC-D) is attributed to the formation of a graphene-like layer in SiC near the interface.

In SiC-D a memory effect is observed at 10 K (Figure 4), where the thermal oxide was replaced by a deposited oxide. A region with high F_D is still present in C-face SiC even after removing the thermally grown SiO_2, suggesting that the oxidation process caused a permanent modification of the SiC crystal, e.g., by emission of oxidation by-products into the SiC crystal. Interestingly, F_D only increases a few nanometers below the SiO_2/SiC interface, suggesting a narrow C-rich layer, as discussed for SiC-C, which was not removed during HF etching,[54] and is still present below the PECVD oxide. However, this difference cannot be solely attributed to the impact of crystal orientation on the oxidation process, as it is indistinguishable from the effect of different doping concentrations on F_D at the surfaces of the semiconductors,
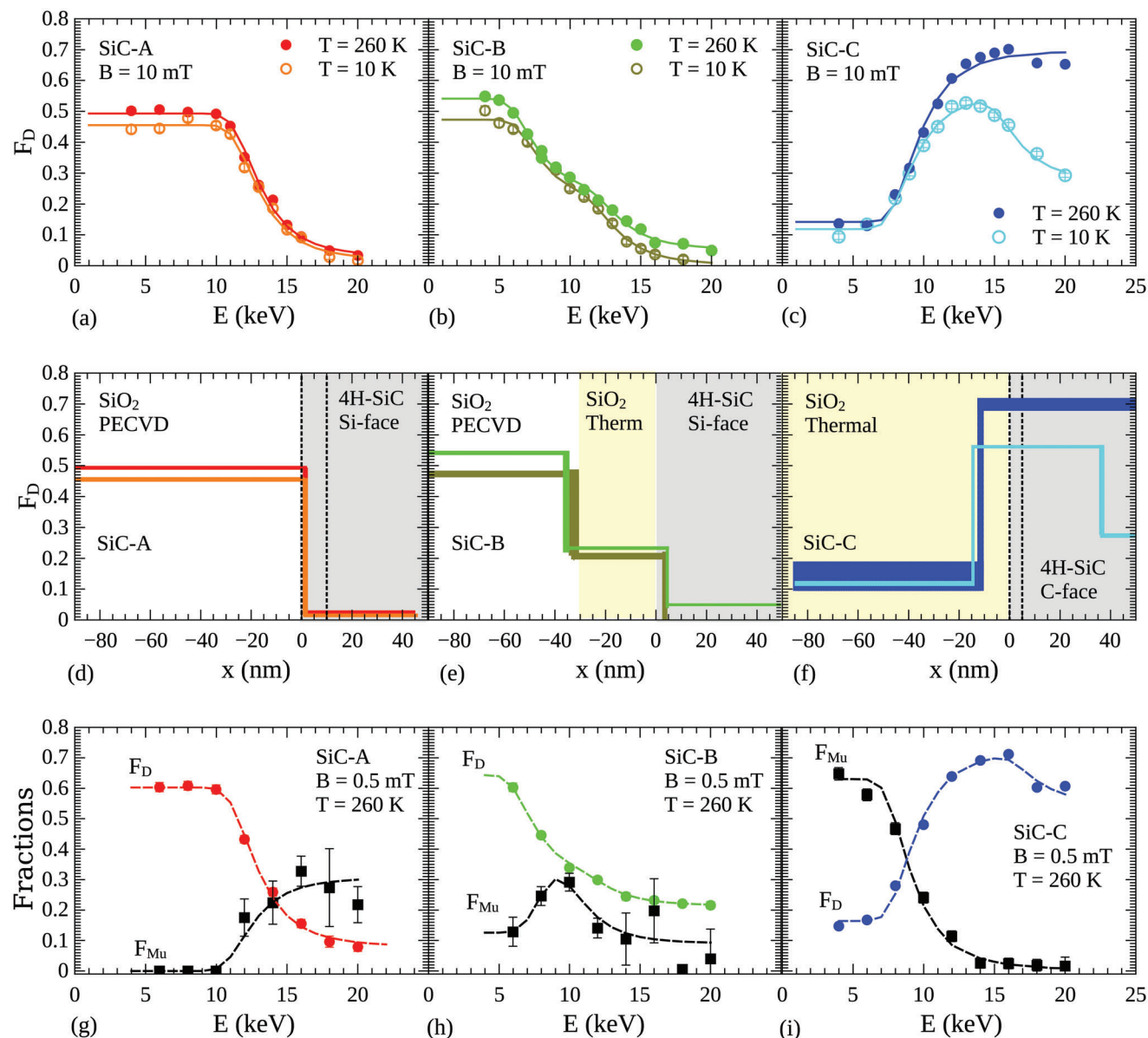
ADVANCED
SCIENCE NEWS
www.advancedsciencenews.com

ADVANCED
MATERIALS
INTERFACES
Open Access
www.advmatinterfaces.de

Figure 3. Analysis of diamagnetic (F_D) and paramagnetic (F_{Mu}) fractions measured for SiC-A, SiC-B, and SiC-C. a–c) F_D as a function of muon implantation energy measured at 10 and 260 K with an externally applied magnetic field of 10 mT. d–f) Depth variation of F_D obtained by fitting the corresponding muon implantation energy dependence. The width of the colored lines indicates the standard deviation of the fit parameters. g–i) F_D and F_{Mu} as function of muon implantation energy measured at 0.5 mT and 260 K. The fitted dashed lines describe the variation of the fractions, assuming $F_D(x)$ and $F_{Mu}(x)$ are abruptly changing between the different layers of the sample.

where SiC-B has three orders of magnitude smaller doping concentration than SiC-C.

2.2.2. Impact of Charge Carrier Concentration

In SiC-A, F_D is nearly temperature-independent (Figure 3a,d) in the SiC crystal where the Mu^0 signal is visible, and the respective fractions in Figure 3g are comparable to similarly doped epitaxial SiC reported by Woerle et al.[24,25] Although the doping concentration of SiC-B is the same as of SiC-A, the thermal oxidation

in SiC-B leads to an unexpected increase of F_D to ≈20% within the semiconductor at 0.5 mT (Figure 3h). Defects related to the carbon vacancy in SiC lead to an increased F_D.[24] Here, it is unlikely that carbon vacancies are responsible for the observations in Figure 3h, since the oxidation process itself is initiated by a Si out-diffusion and only a later destruction of the C sub-lattice.[55] Furthermore, LE-µSR is only sensitive to carbon vacancy concentrations >1×10^{17} cm^{-3}, where ≈30% paramagnetic fraction is still observed. In contrast to SiC-A, the Mu^0 signal disappears in the SiC layer of the SiC-B sample. This can be explained by the interaction with free charge carriers present in SiC near the
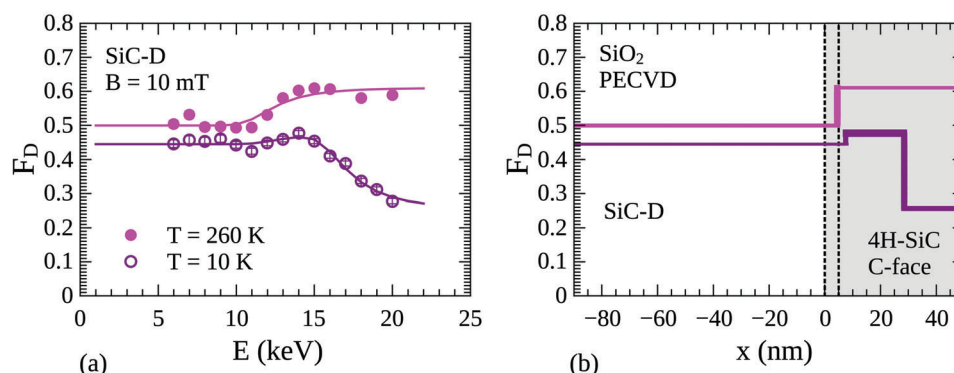
2300209 (6 of 10)

**ADVANCED
SCIENCE NEWS**

www.advancedsciencenews.com

**ADVANCED
MATERIALS
INTERFACES**

Open Access

www.advmatinterfaces.de

Figure 4. a) Analysis of the diamagnetic fraction F_D measured in SiC-D, as function of muon implantation energy at 10 and 260 K with an externally applied magnetic field of 10 mT. b) Depth variation of F_D obtained by fitting the corresponding muon implantation energy dependence. The width of the colored lines indicates the standard deviation of the fit parameters.

interface, after thermal oxidation. The increase of F_D is hardly observable at 10 mT, which suggests that there is a neutral Mu^0 precursor state that quickly dephases.[24] At 0.5 mT, due to the smaller precession frequencies of the muon spin in Mu^0 compared to 10 mT, the contribution of either electron or hole capture by Mu^0 to form Mu^- or μ^+, respectively, can be observed. With LE-μSR, a hole carrier concentration of 1×10^{17} cm^{-3} is required to observe an increase of F_D due to μ^+ by hole capture. This concentration is higher than expected for the n-type SiC even in the case of upward band-bending caused by thermal oxidation.[56] Therefore, we attribute the increase of F_D at 260 K to the presence of electrons from the interface trap states.

The high value of $F_D \approx 55\%$ at 10 K in a 30-nm-wide region inside the semiconductor in highly-doped, C-face SiC (SiC-C and SiC-D) hints toward an electron-rich region near the interface. The graphene layer grown during oxidization at the interface of C-face SiC has been reported to be n-type.[57] The doping is proposed to originate from three different mechanisms, which at times coexist: electron transfer from interface states (Si and C dangling bonds) to the graphene layer, polarization induced by the hexagonal geometry of the 4H-SiC substrate, and the effect of a space-charge region in doped SiC. Additionally, electron exchange with the bulk is also compatible with the C-face SiC substrate doping concentration of 1×10^{19} cm^{-3}.[58,59] At a distance beyond 30 nm from the interface, F_D drops to $\approx 25\%$. This diamagnetic fraction in the "bulk" of the SiC originates from the capture of the majority charge carriers (electrons) by Mu^0. Recently, we measured SiC with various n- and p-doping levels up to 1×10^{18} cm^{-3} with LE-μSR, and we observed a fraction of $F_D \approx 25\%$ corresponding to an electron concentration of $\approx 5 \times 10^{17}$ cm^{-3}.[60] This is much smaller than the bulk doping level of 1×10^{19} cm^{-3}, since at 10 K, only a small fraction of donors is ionized. The increase of F_D - due to Mu^- formation - to ≈ 55 K closer to the interface would then mean that there is a high effective electron density in the 30-nm-wide region of C-face SiC. Considering previously discussed defect formation mechanisms during thermal oxidation, we attribute the change in carrier concentration to the negatively charged graphene-like layer near the interface of the oxidized C-face.

In SiC-C and SiC-D, conversion of F_{Mu} to F_D is visible in the semiconductor at 260 K (Figures 3i and 4b), as the thermal ion-

ization of nitrogen donors takes place at $T > 75$ K, where the availability of free electrons from the ionized donors promote the formation of Mu^- from Mu^0 precursor states. Thus, at 260 K the n-type, C-rich region where F_D is enhanced is no longer distinguishable due to the high concentration of free electrons. This enhanced Mu^- formation at 260 K is the cause for the higher value of $F_D \approx 70\%$ deep (>40 nm) inside the semiconductor, compared to $\approx 25\%$ at 10 K.

3. Conclusion

We set out to investigate the different oxide growth processes on Si and SiC, and their effects on the oxide-semiconductor interface, using depth-resolved LE-μSR. The muon's sensitivity to defects allowed for a clear distinction between the PECVD SiO$_2$ and thermally grown SiO$_2$, due to the higher structural order of the latter. In the samples with PECVD-SiO$_2$ an abrupt transition from the oxide to the semiconductor is observed, whereas samples with thermally grown SiO$_2$ exhibit a near-interface region with enhanced defect density. Effects of the thermal oxidation could be probed with nanometer resolution, and the extension of the defective region on the oxide and semiconductor side was quantified. On the oxide side a 15 to 30 nm wide defective region was observed, owing to a combination of factors such as interface defects, near-interface oxide traps, and oxidation-induced stress. In the case of Si, removing the thermal oxide was shown to also remove the defective layer. In SiC, the near-interface defect layer depends on the polarity of the oxidized face. The changes observed near the interface of the Si- and C-face SiC samples depend on the corresponding bulk carrier concentration and the overall oxidation process, and can be accounted for due to the sensitivity of the muons to the charge carrier concentration. On the Si-face, electron depletion is observed. On the C-face, a C-rich 30 nm defective layer is detected due to its donor behavior, and is still visible after etching the thermal oxide and deposition of PECVD-SiO$_2$.

These results demonstrate the capability of LE-μSR to deliver information about structural and electronic properties of oxide-semiconductor interfaces with hitherto inaccessible sensitivity and depth resolution. Moreover, the depth-dependent analysis and findings presented serve as a baseline for follow-up LE-μSR
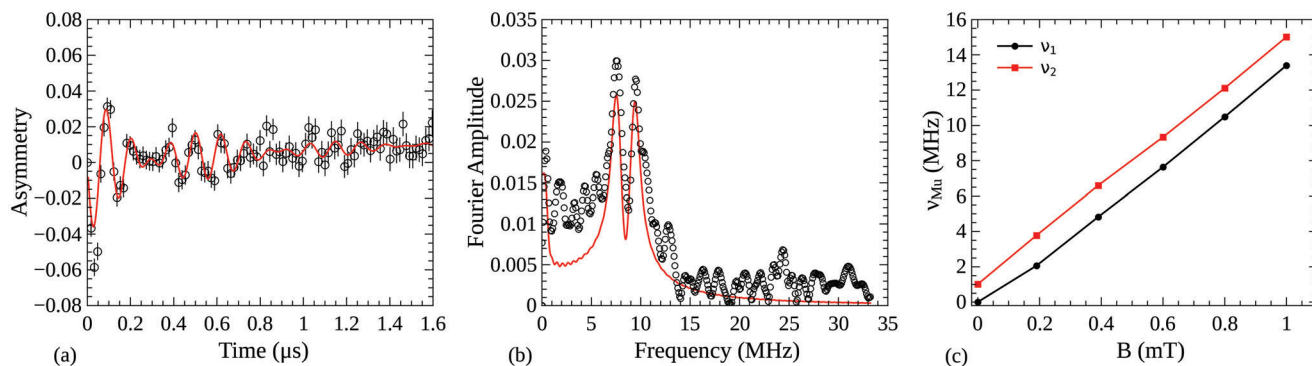
**ADVANCED
SCIENCE NEWS**

www.advancedsciencenews.com

**ADVANCED
MATERIALS
INTERFACES**

www.advmatinterfaces.de

Figure 5. a) Mu^0 asymmetry spectrum in a low-doped 4H-SiC epitaxial layer in an applied field of 0.6 mT. b) Power Fourier spectrum of (a). c) Mu^0 precession frequencies $\nu_{1(2)} = \omega_{1(2)}/2\pi$ as a function of applied field. $\Delta\nu = \nu_2 - \nu_1$ does not change in this field range, which means that $\nu_a = \Delta\nu \ll \nu_{iso}$.

studies on the effect of state-of-the-art processing steps required to improve the interface. A good understanding of interface properties is critical for device operation, and the information provided by LE-μSR can, in turn, advance the development of reliable SiC power devices.

4. Experimental Section

Sample Preparation: For this experiment, (100) silicon with a nitrogen donor concentration of $N_D = 5 \times 10^{16}$ cm^{-3} as well as (0001) Si-face 4H-SiC ($N_D = 8 \times 10^{15}$ cm^{-3}) and (000$\bar{1}$) C-face 4H-SiC ($N_D \approx 1 \times 10^{19}$ cm^{-3}) were used. All samples were cut into sizes of 25 mm × 25 mm and wet-chemically cleaned using full RCA process prior to oxidation. The oxide was either thermally grown at 1050 °C in O_2 ambient or deposited at 300 °C in a PECVD chamber. No post-oxidation annealing or other processes for improving the oxide quality were performed for any of the samples. The final oxide thicknesses were confirmed by profilometer and reflectometer measurements. Two samples, Si-C and SiC-D, were first thermally oxidized before the SiO_2 was removed again by dipping the sample in hydrofluoric acid (HF) and another SiO_2 layer was deposited on the samples. As the oxide growth rate at 1050 °C was very low on the (0001) Si-face of 4H-SiC, only a 30 nm-thick oxide was thermally grown on sample SiC-B and another SiO_2 layer of 70 nm was deposited on top.

Density Measurements: Additional X-ray reflectivity (XRR) measurements were used for the estimation of oxide densities: for thermally grown oxides, a density of $\rho_{SiO2, ther} = 2.2$ g cm^{-3} was extracted, whereas the deposited oxide had a slightly smaller density of $\rho_{SiO2, dep} = 2.1$ g cm^{-3}.

Electrical Characterization: Capacitance–voltage (C–V) and current–voltage (I–V) measurements of the metal-oxide-semiconductor (MOS) capacitors fabricated on the Si-A, Si-B, SiC-A, and SiC-B samples were performed. Circular 200 nm Al contacts with a diameter of 400 μm were deposited on top of the oxide to create the MOS structure. The goal of the electrical characterization was to relate its microscopic analysis with LE-μSR to macroscopic device properties. The density of interface states (D_{it}) were determined from the capacitance and conductance curves obtained at 1MHz.[61] The D_{it} shown in Tables 1 and 2 was extracted at E_C-0.1eV.

μSR Measurements: The LE-μSR experiments were performed at the low-energy muon facility (LEM) located at the μE4 beamline[62] of the Swiss Muon Source (SμS, Paul Scherrer Institute, Villigen, Switzerland). The samples were glued with conductive silver paint onto a Ni-coated aluminum sample plate mounted on a cold-finger cryostat. The muon implantation energy ranged from 4 to 20 keV, probing the first 150 to 190 nm of the SiC and Si samples, respectively. The energy dependent measurements were carried out at temperatures of 10 and 260 K, with transverse magnetic fields of 0.5 and 10 mT applied parallel to the beam axis. At a

magnetic field of 10 mT only the diamagnetic signal could be resolved due to the frequency detection limit of 50 MHz of the instrument. Additionally, at 0.5 mT the precession signal of Mu^0 was detected, where only about 50% of the total polarization was visible.[11] For 10 mT measurements three million low-energy muon events were recorded, and eight million events for 0.5 mT measurements.

The μSR asymmetry spectra were analyzed using the software *musrfit*.[63] At a field of 10 mT, where in this case only the diamagnetic signal with asymmetry A_D was observable, an exponentially-damped cosine function at the Larmor frequency ω_μ of the muon was used to fit the data

$$A(t) = A_D \cdot \exp(-\lambda_D \cdot t) \cdot \cos(\omega_\mu t + \phi_D) \quad (1)$$

where λ_D is the depolarization rate of the diamagnetic state, and ϕ is the phase of the precession signal in a specific positron detector. At 0.5 mT, a second component becomes visible, which is the precession of the paramagnetic Mu^0 state with asymmetry A_{Mu}:

$$A(t) = A_D \cdot \exp(-\lambda_D \cdot t) \cdot \cos(\omega t + \phi_D) \quad (2)$$
$$+ A_{Mu} \cdot \exp(-\lambda_{Mu} \cdot t) \cdot \cos(\omega_{Mu} t + \phi_{Mu})$$

where λ_{Mu} is the exponential depolarization rate of Mu^0, and ω_{Mu} is the muon spin precession frequency in the Mu^0 triplet state.[11] The phases ϕ_D and ϕ_{Mu} of the diamagnetic and paramagnetic LE-μSR signals were determined by the position of a specific positron detector with respect to the initial muon spin direction.

In 4H-SiC, the Mu^0 precession frequency splits into two lines due to a so far unreported weak anisotropy of the hyperfine coupling of $\nu_a \approx 1.7$ MHz on top of the isotropic part with a much larger coupling ν_{iso} of about 3000MHz:

$$A(t) = A_D \cdot \exp(-\lambda_D \cdot t) \cdot \cos(\omega t + \phi_D)$$
$$+ A_{Mu} \cdot \exp(-\lambda_{Mu} \cdot t) \cdot [\cos(\omega_1 t + \phi_{Mu}) + \cos(\omega_2 t + \phi_{Mu})] \quad (3)$$

where $\omega_1 = \omega_{Mu} - 2\pi\nu_a/2$, and $\omega_2 = \omega_{Mu} + 2\pi\nu_a/2$, see **Figure 5**. The isotropic coupling ν_{iso} had been determined in Ref. [64], where the authors indicated the presence of a presumably small anisotropic component in the hyperfine coupling. In the analysis of this data, the splitting of the Mu^0 lines in 4H-SiC allowed distinguishing the fractions of muonium forming in the oxide and in SiC.

μSR Fitting Procedure: The method implemented by Simões et al. takes advantage of the nanometer depth-resolution of the LE-μSR technique to infer the depth variation of the parameters from the experimentally measured energy dependence.[65] In this study, the depth dependence of the diamagnetic fraction was obtained using the correlation of the muon

**ADVANCED
SCIENCE NEWS**

www.advancedsciencenews.com

**ADVANCED
MATERIALS
INTERFACES**

www.advmatinterfaces.de

implantation energy and its stopping depth, the stopping probability $P(x, E)$, calculated via the Monte Carlo simulation TRIMSP[28,29] for all the samples. $P(x, E)$ is the probability per unit length that a muon implanted with energy E stops in the material at a depth x, as shown for different samples in Figure 1.

The fraction F_D of muons with a final diamagnetic state depended on the material, and had distinct characteristic values for the oxide and the semiconductor. Thus, this study assume a step-like function to be a good approximation of the F_D variation within the structure.[17,66]

Conflict of Interest

The authors declare no conflict of interest.

Data Availability Statement

The data that support the findings of this study are available from the corresponding author upon reasonable request.

[1] W. Choyke, G. Pensl, *MRS Bull.* **1997**, *22*, 25.
[2] S. E. Saddow, *Micromachines* **2022**, *13*, 346.
[3] N. T. Son, C. P. Anderson, A. Bourassa, K. C. Miao, C. Babin, M. Widmann, M. Niethammer, J. Ul Hassan, N. Morioka, I. G. Ivanov, F. Kaiser, J. Wrachtrup, D. D. Awschalom, *Appl. Phys. Lett.* **2020**, *116*, 190501.
[4] M. E. Bathen, L. Vines, *Adv. Quantum Technol.* **2021**, *4*, 2100003.
[5] S. M. Sze, K. K. Ng, *Physics of Semiconductor Devices*, Wiley, New York **2007**.
[6] D. K. Schroder, *Semiconductor Material and Device Characterization*, John Wiley & Sons, Inc., Hoboken, New Jersey **2005**.
[7] (Eds: S. Kasap, P. Capper), *Springer Handbook of Electronic and Photonic Materials*, Springer, Berlin **2017**.
[8] B. Hornetz, H. Michel, J. Halbritter, *J. Mater. Res.* **1994**, *9*, 3088.
[9] J. A. Taillon, J. Hyuk Yang, C. A. Ahyi, J. Rozen, J. R. Williams, L. C. Feldman, T. S. Zheleva, A. J. Lelis, L. G. Salamanca-Riba, *Journal of Applied Physics* **2013**, *113*, 044517.
[10] T. Biggerstaff, C. Reynolds Jr., T. Zheleva, A. Lelis, D. Habersat, S. Haney, S.-H. Ryu, A. Agarwal, G. Duscher, *Appl. Phys. Lett.* **2009**, *95*, 032108.
[11] (Eds.: S. J. Blundell, R. D. Renzi, T. Lancaster, F. L. Pratt), *Muon Spectroscopy - An Introduction*, Oxford University Press, Oxford **2021**.
[12] A. D. Hillier, S. J. Blundell, I. McKenzie, I. Umegaki, L. Shu, J. A. Wright, T. Prokscha, F. Bert, K. Shimomura, A. Berlie, H. Alberto, I. Watanabe, *Nat. Rev. Methods Primers* **2022**, *2*, 1.
[13] P. W. Percival, *Radiochim. Acta* **1979**, *26*, 1.
[14] B. D. Patterson, *Rev. Mod. Phys.* **1988**, *60*, 69.
[15] S. F. J. Cox, *Rep. Prog. Phys.* **2009**, *72*, 116501.
[16] D. Eshchenko, V. Storchak, J. Brewer, G. Morris, S. Cottrell, S. Cox, *Phys. Rev. B* **2002**, *66*, 035105.
[17] H. Alberto, R. Vilão, R. Vieira, J. Gil, A. Weidinger, M. Sousa, J. Teixeira, A. Da Cunha, J. Leitão, P. Salomé, P. Fernandes, T. Törndahl, T. Prokscha, A. Suter, Z. Salman, *Phys. Rev. Mater.* **2018**, *2*, 025402.
[18] T. Prokscha, K.-H. Chow, Z. Salman, E. Stilp, A. Suter, *Phys. Rev. Appl.* **2020**, *14*, 1014098.
[19] E. Morenzoni, T. Prokscha, A. Suter, H. Luetkens, R. Khasanov, *J. Phys.: Condens. Matter* **2004**, *16*, 40S4583.
[20] D. Harshman, A. Mills Jr, J. Beveridge, K. Kendall, G. Morris, M. Senba, J. Warren, A. Rupaal, J. Turner, *Phys. Rev. B* **1987**, *36*, 168850.
[21] E. Morenzoni, F. Kottmann, D. Maden, B. Matthias, M. Meyberg, T. Prokscha, T. Wutzke, U. Zimmermann, *Phys. Rev. Lett.* **1994**, *72*, 2793.
[22] E. Morenzoni, H. Glückler, T. Prokscha, H. Weber, E. Forgan, T. Jackson, H. Luetkens, C. Niedermayer, M. Pleines, M. Birke, A. Hofer, J. Litterst, T. Riseman, G. Schatz, *Phys. B: Condens. Matter* **2000**, *289*, 653.
[23] T. Prokscha, E. Morenzoni, C. David, A. Hofer, H. Glückler, Scandella, L, *Appl. Surf. Sci.* **2001**, *172*, 3-4235.
[24] J. Woerle, T. Prokscha, A. Hallén, U. Grossner, *Phys. Rev. B* **2019**, *100*, 11115202.
[25] J. Woerle, M. E. Bathen, T. Prokscha, A. Galeckas, H. M. Ayedh, L. Vines, U. Grossner, *Phys. Rev. Appl.* **2020**, *14*, 5054053.
[26] T. Prokscha, K. H. Chow, E. Stilp, A. Suter, H. Luetkens, E. Morenzoni, G. J. Nieuwenhuys, Z. Salman, R. Scheuermann, *Sci. Rep.* **2013**, *3*, 1.
[27] T. Prokscha, H. Luetkens, E. Morenzoni, G. Nieuwenhuys, A. Suter, M. Döbeli, M. Horisberger, E. Pomjakushina, *Physical Review B* **2014**, *90*, 235303.
[28] W. Eckstein, *Computer Simulation of Ion-Solid Interactions*, Springer Series in Materials Science, Springer, Berlin Heidelberg **1991**.
[29] E. Morenzoni, H. Glückler, T. Prokscha, R. Khasanov, H. Luetkens, M. Birke, E. M. Forgan, C. Niedermayer, M. Pleines, *Nucl. Instrum. Methods Phys. Res., Sect. B* **2002**, *192*, 254.
[30] S. Kreitzman, B. Hitti, R. Lichti, T. Estle, K. Chow, *Phys. Rev. B* **1995**, *51*, 13117.
[31] R. F. Kiefl, J. B. Warren, C. J. Oram, G. M. Marshall, J. H. Brewer, D. R. Harshman, C. W. Clawson, *Phys. Rev. B* **1982**, *26*, 2432.
[32] T. Prokscha, E. Morenzoni, D. Eshchenko, N. Garifianov, H. Glückler, R. Khasanov, H. Luetkens, A. Suter, *Physical review letters* **2007**, *98*, 227401.
[33] N. Funamori, K. M. Kojima, D. Wakabayashi, T. Sato, T. Taniguchi, N. Nishiyama, T. Irifune, D. Tomono, T. Matsuzaki, M. Miyazaki, M. Hiraishi, A. Koda, R. Kadono, *Sci. Rep.* **2015**, *5*, 1.
[34] M. L. Reed, J. D. Plummer, *J. Appl. Phys.* **1988**, *63*, 5776.
[35] Z. Chen, K. Yasutake, A. Doolittle, A. Rohatgi, *Appl. Phys. Lett.* **1993**, *63*, 2117.
[36] K. Queeney, M. Weldon, J. Chang, Y. Chabal, A. Gurevich, J. Sapjeta, R. Opila, *J. Appl. Phys.* **2000**, *87*, 31322.
[37] E. Kobeda, E. Irene, *J. Vac. Sci. Technol. B* **1987**, *5*, 15.
[38] I. Fan, K. Chow, B. Hitti, R. Scheuermann, W. MacFarlane, A. Mansour, B. Schultz, M. Egilmez, J. Jung, R. Lichti, *Phys. Rev. B* **2008**, *77*, 035203.
[39] T. Prokscha, *Phys. Procedia* **2012**, *30*, 50.
[40] Y. Hijikata, H. Yaguchi, S. Yoshida, **2009**, *2*, 021203.
[41] Y. Hijikata, *Diamond Relat. Mater.* **2019**, *92*, 253.
[42] J. M. Knaup, P. Deák, T. Frauenheim, A. Gali, Z. Hajnal, W. J. Choyke, *Phys. Rev. B* **2005**, *72*, 115323.
[43] S. Dhar, S. T. Pantelides, J. R. Williams, L. C. Feldman, in (Eds.: D. M. Fleetwood, R. D. Schrimpf), *Defects in Microelectronic Materials and Devices*, CRC Academic Press, Chap. 20, **2009**.
[44] C. Cochrane, P. Lenahan, A. Lelis, *J. Appl. Phys.* **2011**, *109*, 014506.

[45] M. A. Anders, P. M. Lenahan, C. J. Cochrane, A. J. Lelis, *IEEE Trans. Electron Devices* **2014**, *62*, 301.

[46] J. Hass, W. A. de Heer, E. H. Conrad, *J. Phys.: Condens. Matter* **2008**, *20*, 323202.

[47] M. Yoshikawa, Y. Fujita, M. Murakami, *Appl. Spectrosc.* **2019**, *73*, 1193.

[48] Y. Song, S. Dhar, L. C. Feldman, G. Chung, J. R. Williams, *J. Appl. Phys.* **2004**, *95*, 4953.

[49] H. Hirai, K. Kita, *Appl. Phys. Lett.* **2017**, *110*, 152104.

[50] V. V. Afanas'ev, M. Bassler, G. Pensl, M. J. Schulz, *Phys. Stat. Sol. (a)* **1997**, *321*, 162.

[51] K. Fukuda, W. Cho, K. Arai, S. Suzuki, J. Senzaki, T. Tanaka, *Appl. Phys. Lett.* **2000**, *77*, 866.

[52] Luxmi, N. Srivastava, G. He, R. M. Feenstra, P. J. Fisher, *Phys. Rev. B* **2010**, *82*, 235406.

[53] N. Srivastava, G. He, Luxmi, P. C. Mende, R. M. Feenstra, Y. Sun, *J. Phys. D: Appl. Phys.* **2012**, *45*, 15154001.

[54] B. Johnson, J. Woerle, D. Haasmann, C.-K. Lew, R. Parker, H. Knowles, B. Pingault, M. Atature, A. Gali, S. Dimitrijev, M. Camarda, J. McCallum, *Phys. Rev. Applied* **2019**, *12*, 044024.

[55] J. Woerle, B. C. Johnson, C. Bongiorno, K. Yamasue, G. Ferro, D. Dutta, T. A. Jung, H. Sigg, Y. Cho, U. Grossner, M. Camarda, *Phys. Rev. Mater.* **2019**, *3*, 084602.

[56] H. Watanabe, T. Kirino, Y. Kagei, J. Harries, A. Yoshigoe, Y. Teraoka, S. Mitani, Y. Nakano, T. Nakamura, T. Hosoi, et al., in *Mater. Sci. Forum*, Vol. *679*, Trans Tech Publ, **2011**, pp. 386–389.

[57] S. Kopylov, A. Tzalenchuk, S. Kubatkin, V. I. Fal'ko, *Appl. Phys. Lett.* **2010**, *97*, 112109.

[58] J. Ristein, S. Mammadov, T. Seyller, *Phys. Rev. Lett.* **2012**, *108*, 246104.

[59] A. Pradeepkumar, D. K. Gaskill, F. Iacopi, *Appl. Sci.* **2020**, *10*, 4350.

[60] M. M. Martins, P. Kumar, M. E. Bathen, U. Grossner, T. Prokscha, Investigation of doping and dopant dependence of n-type 4H–SiC with low-energy muon spin spectroscopy, **2023**, In preparation.

[61] E. H. Nicollian, J. R. Brews, *MOS Physics and Technology*, Wiley-Interscience, UK **1982**.

[62] T. Prokscha, E. Morenzoni, K. Deiters, F. Foroughi, D. George, R. Kobler, A. Suter, V. Vrankovic, *Nucl. Instrum. Methods Phys. Res., Sect. A* **2008**, *595*, 317.

[63] A. Suter, B. Wojek, *Physics Procedia* **2012**, *30*, 69.

[64] R. L. Lichti, W. A. Nussbaum, K. H. Chow, *Phys. Rev. B* **2004**, *70*, 165204.

[65] A. F. A. Simões, H. V. Alberto, R. C. Vilão, J. M. Gil, J. M. V. Cunha, M. A. Curado, P. M. P. Salomé, T. Prokscha, A. Suter, Z. Salman, *Rev. Sci. Instrum.* **2020**, *91*, 023906.

[66] M. Curado, J. Teixeira, M. Monteiro, E. Ribeiro, R. Vilão, H. Alberto, J. Cunha, T. Lopes, K. Oliveira, O. Donzel-Gargand, A. Hultqvist, S. Calderon, M. Barreiros, W. Chiappim, J. Leitão, A. Silva, T. Prokscha, C. Vinhais, P. Fernandes, P. Salomé, *Appl. Mater. Today* **2020**, *21*, 100867.